

Squaric acid-based zwitterionic covalent organic framework induces triple synergy for boosted hydrogen peroxide photosynthesis

Received: 25 March 2025

Accepted: 4 September 2025

Published online: 08 October 2025

Check for updates

Chenchen Liu^{1,8}, Xueming Liu^{2,8}, Bing Chen¹, Zifan Li³, Xinwen Ou⁴, Yaobin Lu¹, Yuhao Liu⁵, Chongbei Wu⁶, Shan Yao¹, Yunhai Liu³, Liqun Ye⁷, Bin Han¹✉ & Zhifeng Yang¹

Photocatalytic oxygen reduction reaction offers a sustainable approach for hydrogen peroxide (H₂O₂) synthesis, while the efficiency is limited by the challenge of synergistically optimizing the supply of oxygen, protons, and electrons. Here, by elaborately developing squaric acid-based zwitterionic covalent organic framework (STT COF), we propose a triple synergy strategy for boosting H₂O₂ photosynthesis. The as-prepared STT COF delivers a high H₂O₂ yield of 14356.5 μmol g⁻¹ h⁻¹ in pure water, with a notable apparent quantum yield of 40.0% at 420 nm, roughly 7.9 times that of its charge-neutral counterpart and outperforming other documented systems. Under natural sunlight irradiation, a 5 L H₂O₂ solution (~400 μM) is produced in a continuous flow membrane reactor equipped with STT COF and gas diffusion layers. Mechanism studies demonstrate that STT COF induces a strong donor-acceptor (D-A) interaction to promote electron transfer, undergoes spontaneous hydrogenation for continuous protons and facilitating oxygen uptake in a favorable configuration, collectively creating a triple synergy to boost H₂O₂ photosynthesis.

Hydrogen peroxide (H₂O₂), an eco-friendly oxidizing agent and energy carrier, is a vital and versatile chemical widely utilized in chemical synthesis and environmental remediation¹⁻³. The global H₂O₂ market is projected to grow at a compound annual growth rate (CAGR) of 4.6%, reaching 5.7 million tons by 2028⁴. Currently, the anthraquinone oxidation process conducted at high temperatures dominates industrial H₂O₂ production, accounting for over 95% of global output⁵. An alternative approach involves the direct reaction of H₂ and O₂ catalyzed by noble metal catalysts⁶. However, both methods are burdened

by high costs, significant energy consumption, and pollutant emissions^{7,8}. Moreover, the highly concentrated H₂O₂ produced poses considerable safety risks during storage and transportation⁹, although end-use scenarios often require only dilute solutions (e.g., <0.1 wt% for water treatment)¹⁰. Therefore, it is urgent to develop green and sustainable technologies for on-site, on-demand production of ready-to-use H₂O₂ solutions.

Solar-driven oxygen reduction reaction (ORR) is emerging as a promising technique to produce clean H₂O₂ solution from O₂ and

¹Guangdong Basic Research Center of Excellence for Ecological Security and Green Development, Guangdong Provincial Key Laboratory of Water Quality Improvement and Ecological Restoration for Watersheds, School of Ecology, Environment and Resources, Guangdong University of Technology, Guangzhou, P. R. China. ²School of Metallurgy and Environment, Central South University, Changsha, P. R. China. ³State Key Laboratory of Nuclear Resources and Environment, East China University of Technology, Nanchang, P. R. China. ⁴School of Physics, Zhejiang University, Hangzhou, P. R. China. ⁵Pingyuan Laboratory, College of Chemistry, Zhengzhou University, Zhengzhou, P. R. China. ⁶Hebei Center for Industrial Energy-saving and Pollution Control Research, Hebei Vocational University of Technology and Engineering, Xingtai, P. R. China. ⁷College of Materials and Chemical Engineering, Key Laboratory of Inorganic Nonmetallic Crystalline and Energy Conversion Materials, China Three Gorges University, Yichang, P. R. China. ⁸These authors contributed equally: Chenchen Liu, Xueming Liu. ✉e-mail: hanbin@gdut.edu.cn

water^{11–13}. In the photocatalytic ORR process, H₂O₂ can be produced via a one-step two-electron (2e⁻) route (O₂ + 2e⁻ + 2H⁺ → H₂O₂) or a sequential two-step 2e⁻ one (O₂ + e⁻ → O₂⁻ + e⁻ + 2H⁺ → H₂O₂)^{14,15}. Since O₂ adsorption is the key step of photocatalytic ORR, the affinity and initial configurations of O₂ adsorption are crucial for H₂O₂ generation¹⁶. For instance, Yeager-type O₂ adsorption benefits efficient and selective H₂O₂ photosynthesis via the direct 2e⁻ route¹⁷. Once O₂ is adsorbed, it is transformed into H₂O₂ via proton-coupled electron transfer (PCET)¹⁸. To enhance the efficiency and selectivity of H₂O₂ production, it is essential to achieve a triple synergy in providing O₂, protons, and electrons. Recent studies, such as the one conducted by Han et al., demonstrate that engineered electric fields and hydrophilic surfaces can facilitate the transfer of charges and protons, resulting in enhanced H₂O₂ generation¹⁹. Despite these advancements, simultaneously optimizing all three key factors within a single catalyst remains a challenge, leading to unsatisfactory efficiency in solar-driven O₂-to-H₂O₂ conversion.

Covalent organic frameworks (COFs), as metal-free porous materials with customizable active sites and good visible light absorption, are burgeoning as top candidates for H₂O₂ photosynthesis^{20–23}. Since the seminal work reported in 2020 by Thomas and Van Der²⁴, various strategies such as constructing heterojunctions, donor-acceptor (D-A) engineering, and heteroatom doping have been employed to enhance COFs' performance in H₂O₂ photosynthesis^{25,26}. Nevertheless, nearly all reported COFs feature neutral skeletons, which weakens the interaction with guest molecules like O₂ and hinders synergistic optimization of photocatalytic ORR. Zwitterionic COFs, incorporating equimolar and spatially arranged cationic and anionic groups²⁷, have recently emerged as promising candidates for enhancing charge transfer and guest molecule interaction, offering the potential for a single material to perform multiple functions^{28,29}. Although zwitterionic COFs have shown great promise in gas separation and proton conduction³⁰, their application in H₂O₂ photosynthesis remains largely unexplored, likely due to the challenges in the design of suitable charge groups.

Here, a squaric acid (SQ)-based zwitterionic COF (STT COF) was designed to demonstrate the triple synergy in the photocatalytic ORR process. The resulting STT COF achieves an H₂O₂ yield of 14,356.5 μmol g⁻¹ h⁻¹ in pure water, with an apparent quantum yield (AQY) of 40.0% at 420 nm, outperforming its charge-neutral PTT COF counterpart and the state-of-the-art systems ever reported. To address issues related to oxygen supply and catalyst recovery, a continuous flow membrane reactor incorporating STT COF and gas diffusion layers was further developed, enabling sunlight-driven generation of 5 L of H₂O₂ (400 μM) without external aeration. The produced H₂O₂ can be directly used for the in-situ degradation of emerging organic pollutants via Fenton reactions, demonstrating great promise for practical applications. Experiments and theoretical calculations jointly elucidate the triple synergy mechanism in the zwitterionic structure derived from SQ units, which promotes photogenerated charge transfer, ensures a continuous supply of protons, and facilitates O₂ adsorption in the Yeager-type configuration. These findings underscore how the structural design and variation of zwitterionic COFs synergistically promote the ORR processes, paving a feasible avenue for the practical application of H₂O₂ photosynthesis.

Results

Synthesis and structural characterization of COFs

Squaric acid (SQ) and 4,4',4''-(1,3,5-triazine-2,4,6-triyl) trianiline (TAPT) were elaborately selected as the electron donor and acceptor, respectively, to construct the target zwitterionic COF (STT COF), as illustrated in Fig. 1a. For comparative investigation, SQ was substituted by terephthalaldehyde (PDA) to prepare charge-neutral COF (PTT COF) with an identical electron acceptor (TAPT). According to the powder X-ray diffraction (PXRD) patterns (Fig. 1b), the STT COF

exhibits diffraction peaks at ca. 3.4°, 6.32°, and 27.1°, corresponding to the (100), (110), and (001) facets, respectively. Similarly, the PTT COF shows corresponding peaks at around 2.87°, 5.1°, and 25.9°, respectively (Supplementary Fig. 1). The experimental PXRD data of these COFs closely match the simulated AA stacking model, with Pawley fitting analysis yielding R factors of less than 5% for both unweighted-profile (R_p) and weighted-profile (R_{wp}).

The chemical states of the resultant COFs were then systematically investigated. Solid-state ¹³C nuclear magnetic resonance (¹³C ssNMR) spectra (Fig. 1c) display two peaks at ca. 130 and 170 ppm, which can be attributed to the hydrogen-bonded aromatic carbon and the carbon atoms of the triazine units, respectively³¹. The peak at 152 ppm on PTT COF can be assigned to the carbon atom of the imine (C=N) linkage, while the peak at 118 ppm on STT COF refers to the C-N bond³². Besides, two peaks at 150 and 175 ppm are observable at STT COF, corresponding to the C atoms of SQ units. Fourier transform infrared (FTIR) spectra (Supplementary Fig. 2) show the disappearance of amino group peaks (3352–3432 cm⁻¹) and the emergence of C=N bonds (1595 cm⁻¹) after the Schiff base reaction. For STT COF, the enol peak of SQ (2420 cm⁻¹) vanishes, accompanied by a new signal of C-N-C bond (1388 cm⁻¹), whereas the aldehyde peak of PTT COF (2680–2840 cm⁻¹) disappears. According to the X-ray photoelectron spectroscopy (XPS) survey spectra (Supplementary Fig. 3a), C, N, and O are the primary elements of these two COFs. Both C 1s spectra exhibit two distinctive peaks at 284.7 eV and 286.4 eV, corresponding to the sp² carbon and C=N bonds, respectively. Besides, peaks at 285.6 and 287.1 eV in the C 1s spectra of STT COF belong to C-N/C-O and C=O bonds, respectively (Supplementary Fig. 3b)³³. As for N 1s spectra, two peaks at ca. 398.8 and 400.4 eV can be detected (Supplementary Fig. 3c), which are attributed to the C-N=C and hybridized -C=N-, respectively³⁴. Noticeable differences in their O 1s spectra (Fig. 1d), in which distinct signals for O=C and O-C are observable on STT COF, but only small signals ascribed to the adsorbed O₂ on PTT COF. The obtained results clearly confirm the successful fabrication of the targeted COFs.

The microstructural features of these two COFs were characterized by scanning electron microscopy (SEM) and transmission electron microscopy (TEM). As shown in SEM images (Supplementary Fig. 4a–d), both PTT COF and STT COF are composed of irregular and uniform nanorods, respectively. Their morphology was further validated by TEM images (Fig. 1e and Supplementary Fig. 5). According to N₂ adsorption-desorption isotherms (Supplementary Fig. 6a, b), the Brunauer–Emmett–Teller (BET) surface areas of PTT COF and STT COF were calculated to be 1017.1 m² g⁻¹ and 217.9 m² g⁻¹, respectively, along with the average pore size of ca. 3.0 and 2.5 nm (Supplementary Fig. 6c, d). As shown in Fig. 1f, the ultraviolet–visible (UV–vis) absorption spectra from diffuse reflectance reveal that STT COF exhibits a broader absorption in the visible light range than PTT COF, with their bandgaps of 1.97 eV and 2.66 eV, respectively (Supplementary Fig. 7). Based on the Mott–Schottky plots (Supplementary Fig. 8a, b), the conduction band (CB) edges of PTT COF and STT COF are calculated to be -0.80 and -0.46 V (vs. NHE), respectively (Fig. 1g), which are thermodynamically favorable for ORR (O₂ + 2H⁺ + 2e⁻ → H₂O₂, E_{NHE} = 0.68 V).

H₂O₂ photosynthesis and its practical application

The H₂O₂ photosynthesis performance of these two COFs was evaluated in pure water. As shown in Fig. 2a, under visible light irradiation (Xe light, 420 nm < λ < 780 nm), PTT COF delivers an almost steady H₂O₂ generation during the 1-h operation with a moderate rate of 1503.4 μmol h⁻¹ g⁻¹, while STT COF exerts a 6.7-fold enhancement (10,004.2 μmol h⁻¹ g⁻¹) under the identical conditions. Despite comparable light adsorption nature at 420 nm, STT COF still shows about sevenfold higher H₂O₂ yield than PTT COF (Supplementary Fig. 9), signifying that light absorption is not the key factor for differentiating their performance. All the monomers are almost inactive for

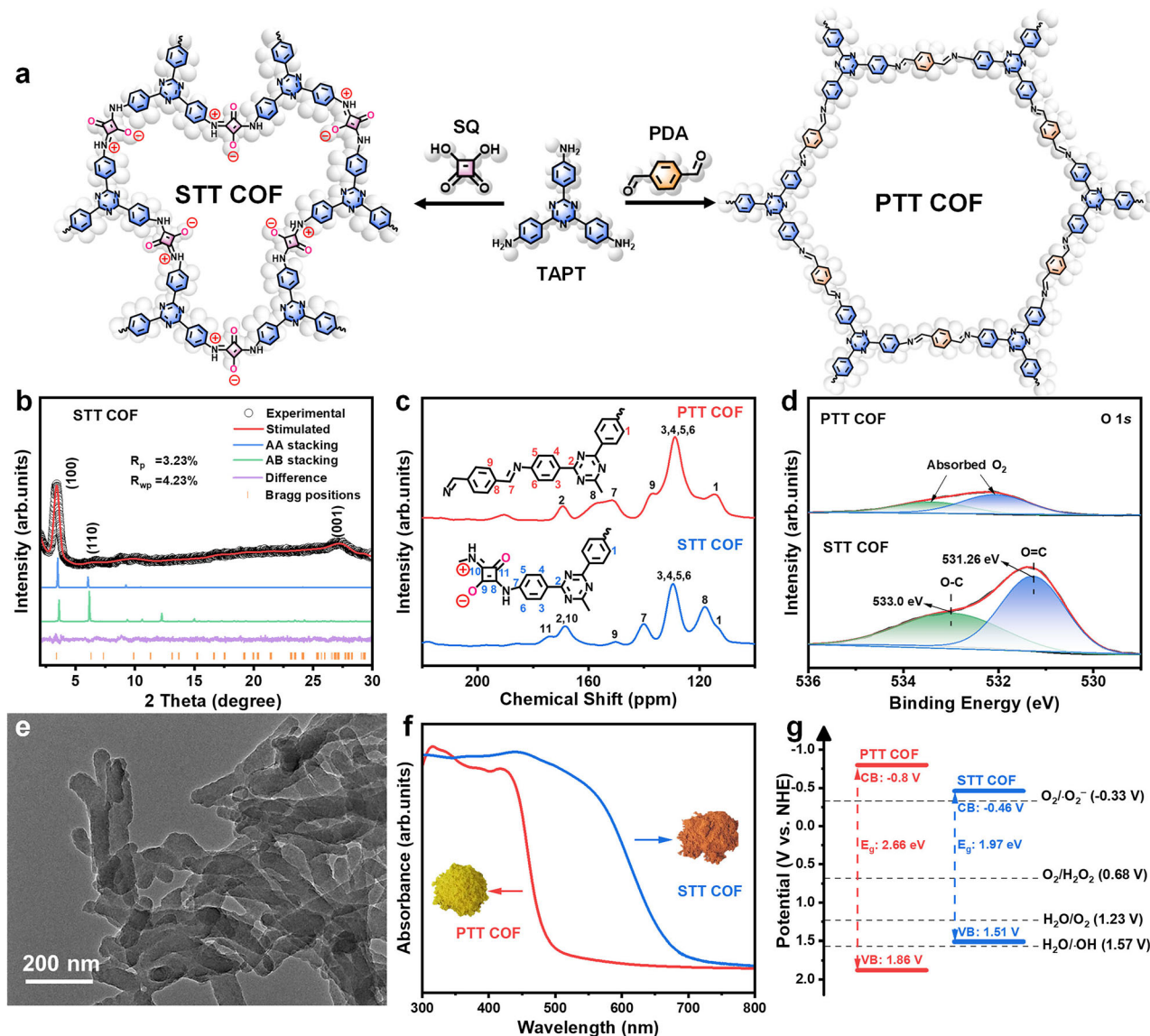


Fig. 1 | Synthesis and structural characterization of COFs. **a** Schematic illustration of the synthesis process of PTT COF and STT COF. **b** The experimental PXRD data and stimulated patterns of STT COF. **c** ^{13}C ssNMR spectra of PTT COF and STT

COF. **d** XPS spectra of O 1s of PTT COF and STT COF. **e** TEM image of STT COF. **f** Ultraviolet-visible absorption spectra from diffuse reflectance of the resultant COFs. **g** Band structure diagrams for PTT COF and STT COF.

H_2O_2 photosynthesis (Supplementary Fig. 10a), highlighting the crucial role of COF structure. As shown in Supplementary Fig. 10b, the slightly increased H_2O_2 content suggests that H_2O_2 decomposition is unlikely to account for their different photocatalytic activity. The optimal dosage of STT COF was found to be 0.25 g L^{-1} (Supplementary Fig. 10c), as both lower and higher concentrations may hinder effective O_2 and light utilization³⁵. Furthermore, STT COF exhibits high compatibility with water matrices and can efficiently produce H_2O_2 from a range of water sources, including tap water, seawater, and Pearl River water (Supplementary Fig. 11). Under UV-vis light irradiation ($320\text{ nm} < \lambda < 780\text{ nm}$), STT COF exerts a high H_2O_2 yield of $14356.5\text{ }\mu\text{mol g}^{-1}\text{ h}^{-1}$ with an apparent quantum yield (AQY) of 40.0% at 420 nm (Fig. 2b), which is 7.9 times higher than that of PTT COF (Supplementary Fig. 12) and surpasses other reported systems in pure water (Supplementary Table 1), demonstrating its notable meliority in this arena. Of note, the produced H_2O_2 can be utilized directly to eliminate contaminants (e.g., methylene blue and bisphenol A) via Fenton reactions (Fig. 2d and Supplementary Fig. 13). Cycling experiments and corresponding characterizations (e.g., PXRD and FTIR analyses, Supplementary

Figs. 14 and 15) jointly validate the good stability of STT COF in this system.

A series of experiments was then conducted to investigate the reaction pathways. As demonstrated in Fig. 2c, almost no H_2O_2 could be detected under dark conditions, in an N_2 -saturated solution or N_2 -saturated KBrO_3 (electron scavenger) solution, while the addition of isopropanol (IPA, hole scavenger) boosted H_2O_2 production. These results suggest that H_2O_2 comes from the photocatalysis-driven ORR process rather than the hole-driven water oxidation reaction (WOR). As revealed in Supplementary Fig. 17, the H_2O_2 production in both COF systems remains nearly unaffected by *p*-benzoquinone (0.01–0.05 mM), suggesting a direct one-step 2e^- ORR pathway¹⁷. Based on the results of rotating ring-disk electrode (RRDE) measurements, STT COF exhibits a lower onset potential, higher H_2O_2 current, and an electron transfer number closer to 2 than PTT COF (Supplementary Fig. 18), which benefits the 2e^- ORR pathway. In the N_2 -saturated KBrO_3 solution, the concentration of dissolved O_2 increases as the reaction proceeds (Supplementary Fig. 19), suggesting that the photogenerated holes oxidize H_2O to yield O_2 . As illustrated in

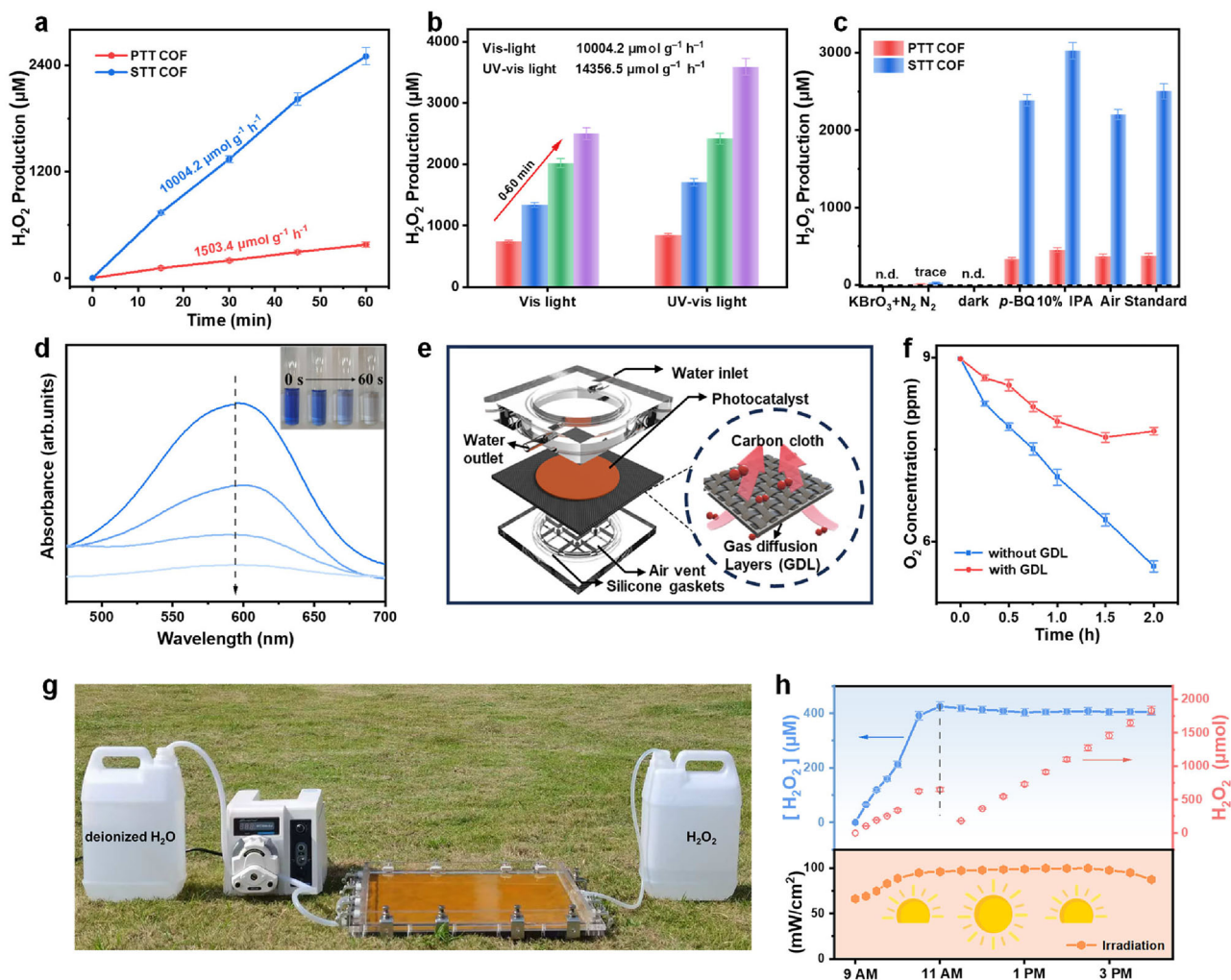


Fig. 2 | Photocatalytic performance of H₂O₂ production and practical application of the as-prepared COFs. **a** Photocatalytic activity of PTT COF and STT COF for H₂O₂ generation in pure water without any sacrificial agents. Conditions: water (20 mL), catalyst (5 mg), visible light, 420 nm < λ < 780 nm. **b** Comparison of photocatalytic H₂O₂ concentration and yield from STT COF under 300 W Xe lamp at different wavenumbers (visible light, 420 nm < λ < 780 nm; UV-vis light, 320 nm < λ < 780 nm). **c** Comparison of H₂O₂ production activities of COFs under various conditions over 1 h, including standard, air, dark, N₂, N₂ + KBrO₃ (10 mM), 10% IPA

and *p*-BQ (0.01 mM). **d** Degradation of methyl blue via Fenton reaction with H₂O₂ produced by STT COF. **e** Labelled diagram of the continuous flow membrane reactor. **f** Experiment on the effectiveness of gas diffusion layers under UV-vis light irradiation. **g** A photograph of the continuous flow membrane reactor under natural sunlight irradiation. **h** The performance of a continuous flow reactor under natural sunlight. The error bars in the figures represent the standard deviations from triplicate tests.

electron paramagnetic resonance (EPR) spectra (Supplementary Figs. 19 and 20), no typical signal for radicals (such as O₂⁻ and ·OH) can be detected in these two COF systems, further excluding the generation of radicals, which aligns closely with quenching experiment results. ¹⁸O₂ isotope experiments were then conducted to confirm the reaction pathways of STT COF. In the STT COF system filled with ¹⁸O₂, the ¹⁶O₂ content remained negligible after 1 h (Supplementary Fig. 21a), corroborating the good airtightness of the reaction system. After 6 h of light illumination, the ¹⁶O₂ level in the STT COF system escalates because of O₂ being produced by 4e⁻ WOR. As depicted in Supplementary Fig. 21b, both ¹⁸O₂ and ¹⁶O₂ were detected after H₂O₂ decomposition, with ¹⁸O₂ as the predominant species (78.7%), further validating the origin of H₂O₂ from the ORR process.

The practical implementation of H₂O₂ photosynthesis is now hindered by the quick consumption of the dissolved O₂ in water and the challenge of catalyst recovery³⁶. Considering the boosted performance of STT COF, a continuous flow membrane reactor with carbon cloth equipped with gas diffusion layers (GDL) and the sample layer on different side (Fig. 2e) was constructed to further evaluate its potential

for practical application. Under UV-vis light irradiation (320 nm < λ < 780 nm) for 2 h, the O₂ concentration in the GDL-free reactor dropped (ca. 33%), but it remained almost unchanged in the GDL-based system (Fig. 2f), demonstrating the efficient O₂ permeability of GDL. In a laboratory-grade reactor (d = 10 cm, h = 2.5 cm, Supplementary Fig. 22a, b), 1.5 L of H₂O₂ solution with a concentration of ca. 250 μM can be produced during a 14-h operation with a flow rate of 2 mL min⁻¹ (Supplementary Fig. 22c). Then, the volume of the reactor was further expanded (40 × 40 × 2 cm) and its performance was evaluated under natural sunlight irradiation, as displayed in Fig. 2g. On August 8th, 2024 with sunny weather, the light intensity at the campus of Guangdong University of Technology was between 65 and 100 mW cm⁻² (Fig. 2h). During a reaction period from 11 AM to 4 PM, H₂O₂ could be continuously produced with a flow of 15 mL min⁻¹, and 5 L of H₂O₂ solution (ca. 400 μM) was finally harvested, which ranks among the top of the documented systems under similar conditions (Supplementary Table 2), highlighting the great practical potential of both STT COF and the continuous flow membrane reactor.

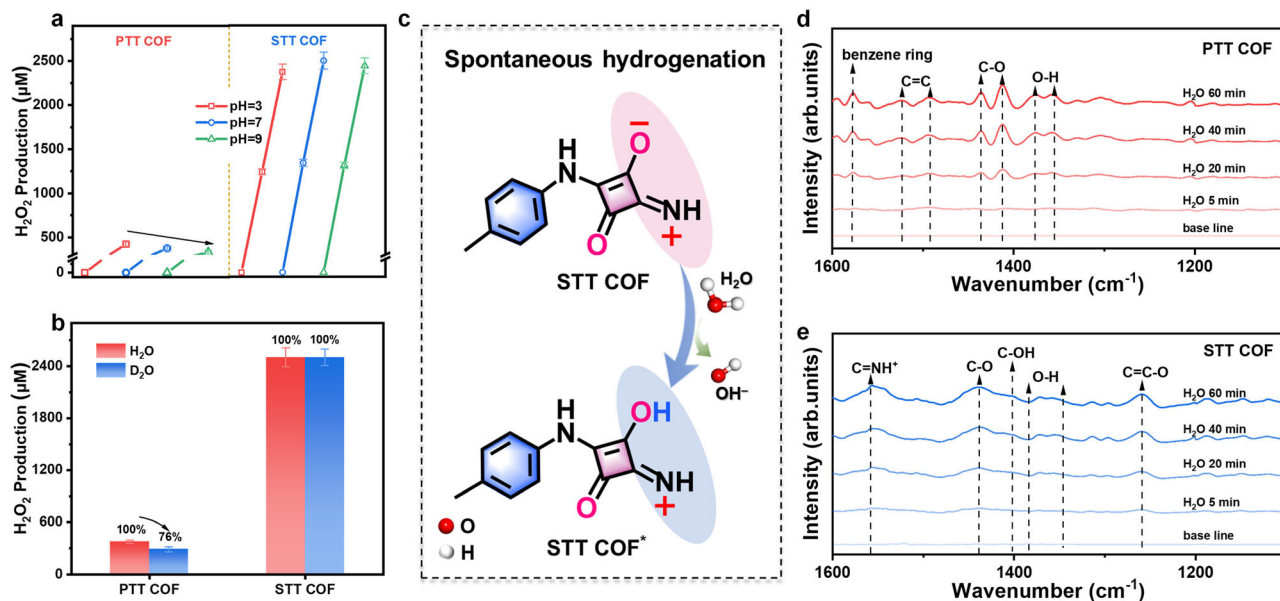


Fig. 3 | Proton utilization ability and the spontaneous hydrogenation process. **a** Photocatalytic H₂O₂ evolution by STT COF and PTT COF under different pH. **b** Photocatalytic activity of STT COF and PTT COF for H₂O₂ generation in H₂O and D₂O. **c** Schematic diagram of the spontaneous hydrogenation process of STT COF.

d In-situ DRIFT spectra of PTT COF and **e** STT COF under dark conditions with continuous water vapor. The error bars in the figures represent the standard deviations from triplicate tests.

Identification of active sites

The effects of SQ units were examined by evaluating the H₂O₂ generation of both COFs under varying pH levels. As shown in Fig. 3a, the activity of PTT COF declines as pH elevates, while the performance of STT COF is virtually unaffected by pH changes. Given that H₂O₂ photosynthesis is a PCET-mediated ORR process, the aforementioned disparity demonstrates that including SQ units considerably enhances the proton utilization capacity of STT COF³⁷. To further evaluate the proton utilization capacity of SQ units, the pH variations of these two COF systems were tested. During the 1-h photocatalytic H₂O₂ production process, the pH of the STT COF-based system increases from 8.16 to 9.17 (Supplementary Fig. 23a), whereas it remains mostly unchanged in the PTT COF-based system. This discrepancy may be attributed to the enhanced ability of STT COF to extract protons from water during the photocatalytic process. Notably, in the dark, the pH of the PTT COF-based system stays mostly stable whereas it gradually increases in the STT COF-based one (Supplementary Fig. 23b). The pH variation of the former can be caused by the negatively charged O atom at the C-O⁻ site in SQ units absorbing protons from water by spontaneous hydrogenation (STT COF → STT COF'), which also results in a structural change (from C-O⁻ to C-OH), as schematically illustrated in Fig. 3c. Since the D-O bond in D₂O is more thermodynamically stable than the H-O bond in H₂O³⁸, it may be harder for COFs to break the D-O bond and extract D⁺ from D₂O. Therefore, photocatalytic hydrogen peroxide production tests using these two COFs were carried out in H₂O and D₂O, respectively. As revealed in Fig. 3b, the activity of PTT COF in D₂O decreased by 24% compared to H₂O, while STT COF delivers almost unchanged performance. Besides, the slightly smaller water contact angle and more negative Zeta potential of STT COF (Supplementary Fig. 24) also reflect facilitated proton uptake by STT COF. Therefore, these findings jointly demonstrate that the SQ units promote proton utilization, which benefits H₂O₂ photosynthesis.

To further substantiate the above hypothesis, in-situ diffuse reflectance infrared Fourier transform spectroscopy (in-situ DRIFT) was performed. In dark with continuous water vapor aerated conditions (Fig. 3d), peaks from C=C stretching modes of benzene ring (1492 and 1523 cm⁻¹) and benzene ring (1573 cm⁻¹) could be observed in PTT COF^{39,40}, and their intensity gradually increased with time,

implying that water is inclined to be adsorbed on the benzene ring in PTT COF. The intensifying peaks of C-O (1414 and 1441 cm⁻¹) and O-H (1354 and 1384 cm⁻¹) may originate from the adsorbed water^{41,42}. As for STT COF (Fig. 3e), the peaks at 1259 cm⁻¹ and 1558 cm⁻¹ are attributed to the C=C-O and C=NH⁺ vibrations⁴³, respectively, while the peak at 1441 cm⁻¹ may come from the vibration of SQ units or adsorbed water. The emerging prominent peak at 1402 cm⁻¹ can be ascribed to the C-OH vibration⁴⁴, further validating the spontaneous hydrogenation process of STT COF (STT COF → STT COF'), which is accompanied by the structural transformation from C-O⁻ to C-OH.

Investigation of exciton and oxygen adsorption behaviors

To disclose the disparities in their H₂O₂ photosynthesis performances, the exciton dissociation and subsequent electron transfer behaviors of these two COFs were thoroughly investigated. Temperature-dependent photoluminescence (TD-PL) spectra were employed to analyze the exciton binding energy (E_b), a crucial parameter that characterizes the Coulomb interaction of excitons and illustrates the energy needed to ionize excitons into free charge carriers⁴⁵. Arrhenius fitting of temperature-dependent integrated PL intensities yields E_b of 83.58 meV for PTT COF and 73.14 meV for STT COF (Fig. 4a, b). The decreased E_b (12%) indicates better exciton dissociation in STT COF⁴⁶. Besides, the intensity of steady-state photoluminescence (PL) spectra of STT COF is much lower than that of PTT COF (Fig. 4c), with an increased average carrier lifetime from 0.787 ns to 1.550 ns (Supplementary Fig. 25), further signifying that the SQ units can significantly suppress the recombination of photogenerated electron-hole (e⁻h⁺) pairs. STT COF exerts a higher photocurrent density than PTT COF (Fig. 4d), indicating more efficient charge separation⁴⁷. The lower charge transference resistance of STT COF obtained by electrochemical impedance spectroscopy (Fig. 4e) implies a lower charge transfer barrier, and the higher surface potential of STT COF determined by Kelvin probe force microscopy (KPFM) test (Fig. 4f) validates its better separation of photogenerated e⁻h⁺ pairs.

Then, femtosecond transient absorption (fs-TA) spectroscopy was carried out to investigate exciton dynamics and carrier transfer mechanisms. As displayed in the two-dimensional (2D) pseudocolor mapping TA spectra and TA spectra signals (Fig. 4g, h and

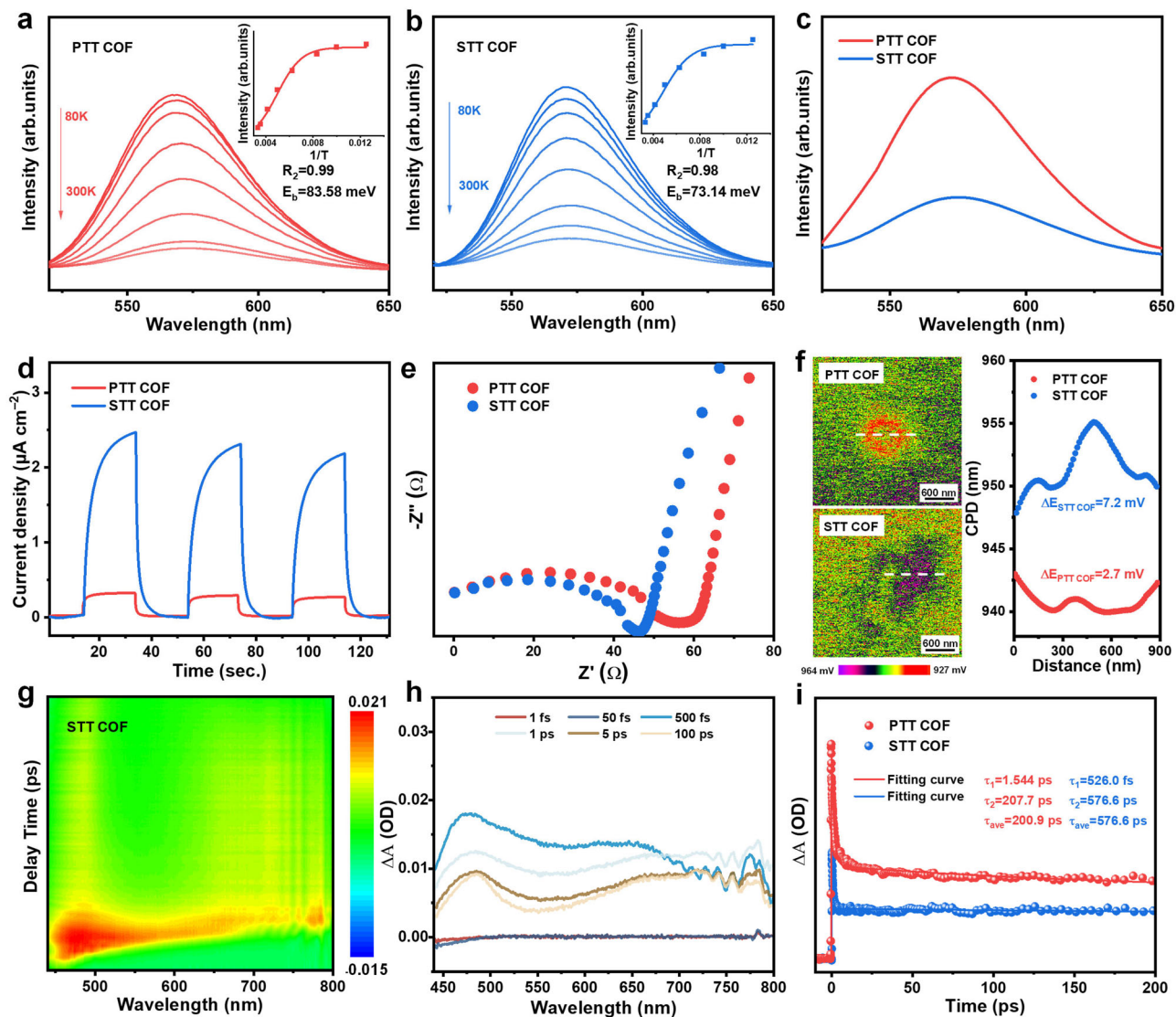


Fig. 4 | Exciton dissociation and electron utilization investigation. **a** STT COF and **b** PTT COF (inset: the relationship between PL intensity and temperature, fitted using the Arrhenius equation). **c** Photoluminescence emission spectra of PTT COF and STT COF. **d** Transient photocurrent under visible light irradiation. **e** Electrochemical impedance spectra (EIS) under visible light irradiation. **f** Images

of KPFM surface potentials (left) of PTT COF and STT COF. Contact potential difference (CPD) (right) of two COFs measured by KPFM. **g** 2D pseudocolor mapping TA spectra of STT COF. **h** TA spectra signals of STT COF. **i** TA kinetics plots and typical fitting curves of PTT COF and STT COF probed at 485 nm probe wavelength.

Supplementary Fig. 26), both PTT COF and STT COF exhibit broad positive absorption between 440 nm and 800 nm, corresponding to excited state absorption signals from electronic transitions between the singlet state (S_1) and higher energy excited states (S_n)⁴⁸. Fig. 4i depicts the TA kinetics of these two COFs at a detection wavelength of 485 nm. Based on the decay curves of the TA signals fitted by a double exponential function (with τ_1 attributed to $S_n \rightarrow S_1$ and τ_2 corresponding to $S_n \rightarrow$ ground state (S_0)⁴⁹, the average lifetime (τ_{ave}) of PTT COF and STT COF is calculated to be 200.9 ps and 576.6 ps, respectively. The longer τ_{ave} indicates that STT COF features an enhanced charge separation capability with a reduced recombination rate⁵⁰. Therefore, introducing SQ units into COF promotes exciton dissociation and then enhances charge separation and transfer efficiency.

In-situ DRIFT was used to identify the real-time intermediates and pathways in H_2O_2 photosynthesis. Under O_2 -saturated conditions with water vapor and visible light irradiation, the benzene ring in PTT COF exhibits characteristic C=C stretching vibrations (Supplementary Fig. 27a), with increasing intensity over time, indicating its role as the catalytic active site. On the other hand, the C=NH⁺ vibration peak in

STT COF (Supplementary Fig. 27b) shows a continuously augmented intensity, indicating that SQ units actively participate in ORR. Besides, distinct peaks attributed to the 1,4-endoperoxide intermediate (910 cm^{-1}) and the -O-O- bond (ca. $1115\text{--}1295\text{ cm}^{-1}$) can be gradually observed in both systems⁵¹, implying their Yeager-type O_2 adsorption configuration, which favors H_2O_2 photosynthesis via a direct one-step $2e^-$ pathway. Besides, the stronger -O-O- signal in STT COF indicates its enhanced O_2 adsorption affinity, which is further validated by the results of O_2 temperature-programmed desorption (O_2 -TPD) (Supplementary Fig. 28).

Theoretical calculations

Time-dependent density functional theory (TD-DFT) and Density functional theory (DFT) calculations were performed to gain an in-depth understanding of the H_2O_2 photosynthesis process over these two COFs (atomic coordinates provided in the Supplementary Data 1 file). Based on the minimum periodic structural units, the highest occupied molecular orbital (HOMO) and lowest unoccupied molecular orbitals (LUMO) for these two COFs were calculated. As displayed in

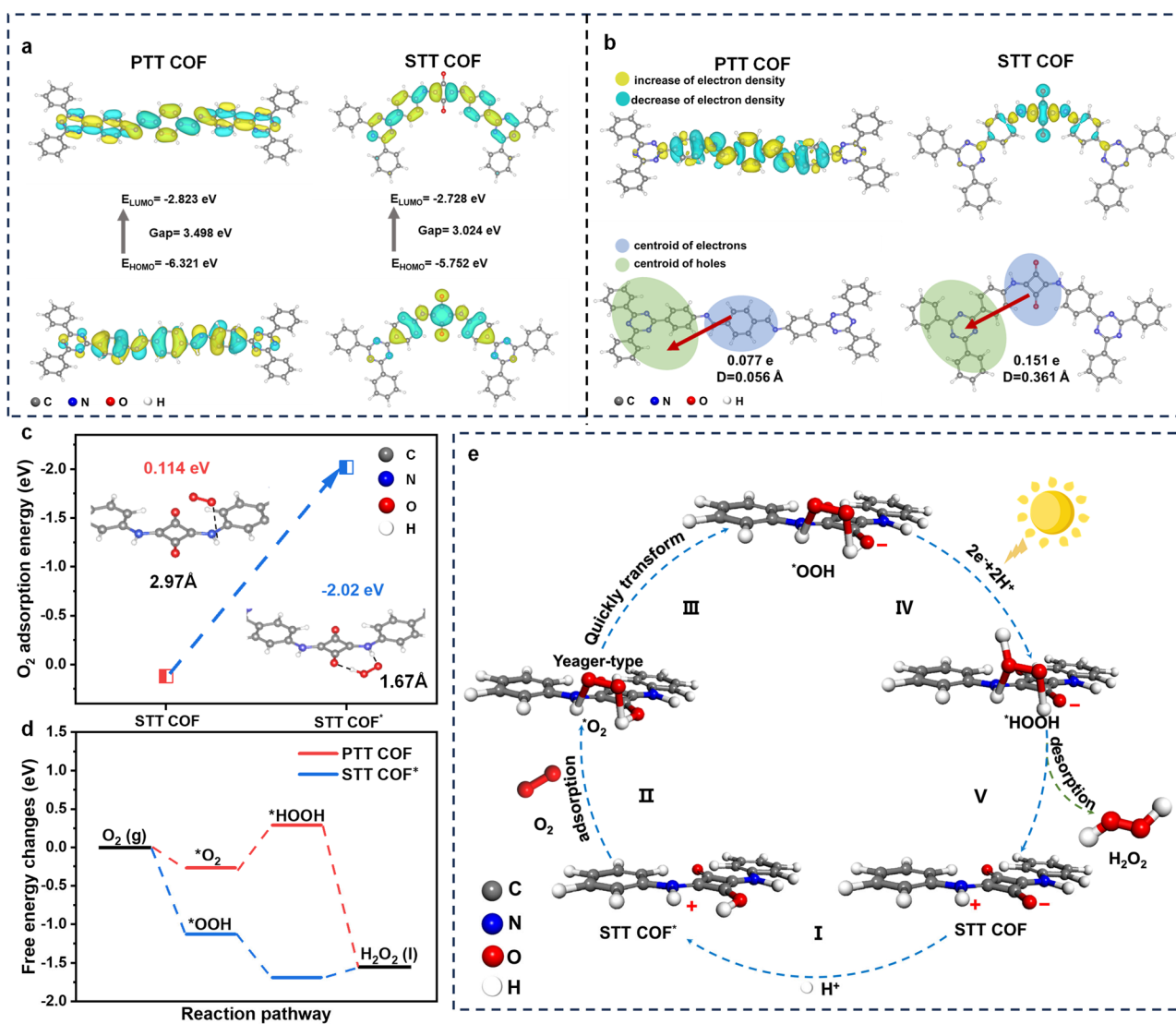


Fig. 5 | TD-DFT calculations and mechanism analysis. **a** Calculated HOMO-LUMO distribution of PTT COF and STT COF. **b** Above: calculation of the charge density difference between the ground and excited states of PTT COF and STT COF. **c** The

adsorption energy of O_2 on the optimum sites of STT COF and STT COF*. **d** Free-energy diagrams for the reduction of O_2 to H_2O_2 on PTT COF and STT COF*. **e** The mechanism of STT COF for photocatalytic H_2O_2 formation.

Fig. 5a, the HOMO and LUMO of PTT COF overlap distinctly, while STT COF exhibits a pronounced spatial separation between HOMO and LUMO, which is conducive to more efficient charge separation upon photoexcitation⁵². Then, the charge density difference between the ground and excited states is analyzed to give insights into their different electron transfer characteristics. The charge transfer distance (D) denotes the distance between the centers of electron density accumulation and depletion zones formed by electronic excitation, reflecting the separation efficiency of e^-h^+ pairs and the spatial separation of orbitals in this D-A system⁵³. As depicted at the top of Fig. 5b, the TAPT unit exhibits its electron-accepting nature, while the SQ and PDA units feature electron-donating properties, signifying clear D-A interactions in these two COFs. The direction and magnitude of charge transfer can be determined through charge density difference and Bader charge calculation, with the corresponding results visualized through the centroids of the electron and hole clouds. As shown in Fig. 5b, STT COF exhibits a larger D (0.361 Å) and transferred charge (0.151 e) than PTT COF (0.056 Å, 0.077 e). The larger D implies the enhanced spatial separation between electron and hole centroids, as well as a stronger D-A interaction, which facilitates charge migration. In STT COF, the SQ units serve as stronger donors, promoting

charge migration toward the TAPT acceptors⁵⁴. Therefore, these calculation results suggest that the SQ units in STT COF facilitate the separation and transfer of photogenerated charges, aligning well with experimental observations.

The adsorption of O_2 molecules on the surface of catalysts is the initial step of the ORR process, which has been then simulated based on the model fragments (Supplementary Fig. 29). As shown in Supplementary Fig. 30, the benzene ring on TAPT units features an enhanced O_2 adsorption energy (-0.099 eV) than the other sites in PTT COF, corresponding to a Yeager-type adsorption configuration, which is consistent with the results of in-situ DRIFT. As for STT COF (Supplementary Fig. 31), the adsorption energies of O_2 on all possible adsorption sites are positive, and the potential adsorption site ($C=NH^+$) features a Pauling-type O_2 adsorption configuration. Neither the O_2 adsorption energies nor configurations match the results of H_2O_2 photosynthesis performance, O_2 -TPD, and in-situ DRIFT. Such a discrepancy motivated further theoretical and experimental investigations. Since the spontaneous sites formed during the reaction may serve as active centers¹⁸, the O_2 adsorption process on the STT COF* (STT COF after the spontaneous hydrogenation) was further investigated. As displayed in Fig. 5c, after converting $C-O^-$ to $C-OH$, STT COF*

offers a pair of adjacent H sites (from C=NH⁺ and C-OH groups, respectively) for O₂ adsorption. The adsorbed O₂ with Yeager-type configuration rapidly acquires H⁺ from the C-OH site and transforms into [•]OOH, which can serve as a metastable O₂-adsorption configuration due to the presence of a hydrogen bond between STT COF and the [•]OOH, as illustrated in Supplementary Video 1. Such an O₂ adsorption configuration features an increased adsorption energy (−2.02 eV), which can be supported by the aforementioned experimental results. Therefore, the C=NH⁺ and C-OH sites in STT COF⁺ instead of the sites in pristine STT COF serve as the actual adsorption centers, implying that the spontaneous hydrogenation of STT COF is capable of boosting O₂ uptakes.

The ORR process over these two COFs was then simulated to understand the reaction pathways from a thermodynamic perspective. PTT COF follows the conventional one-step 2e[−] pathway for H₂O₂ production. As shown in Fig. 5d, the conversion of adsorbed O₂ into intermediates ([•]O₂ → [•]HOOH) serves as the rate-determining step, with an energy barrier (ΔG) of 0.56 eV. As for STT COF⁺, the adsorbed O₂ (i.e., [•]OOH) undergoes a thermodynamically favorable process to form [•]HOOH, which is eventually desorbed to give free H₂O₂ with a small barrier (ΔG) of 0.14 eV ([•]HOOH → H₂O₂(l)). During the whole reaction process, the lower ΔG in STT COF⁺ favors H₂O₂ generation, suggesting the importance of the spontaneous hydrogenation in STT COF for photocatalytic production of H₂O₂.

Based on the above experimental and theoretical results, plausible mechanisms for photocatalytic H₂O₂ production over these two COFs are proposed. STT COF with enhanced D-A configuration can improve the separation of photogenerated e[−]-h⁺ pairs. Moreover, as illustrated in Fig. 5e, the SQ units in STT COF undergo a spontaneous hydrogenation under aqueous conditions, converting the pristine C-O[−] to C-OH (STT COF → STT COF⁺), providing a pair of adjacent H sites to facilitate O₂ adsorption in Yeager-type configuration with lower O₂ adsorption energy. Then the adsorbed O₂ quickly captures the H⁺ from the spontaneous C-OH site to form [•]OOH. Subsequently, the [•]OOH further gains electrons and a proton via a one-step 2e[−] to produce [•]HOOH. After generating H₂O₂ via [•]HOOH desorption, the original STT COF state is regenerated from STT COF⁺ and rolls for the next photocatalytic cycle. On the other hand, as for PTT COF, the adsorbed O₂ on the benzene ring on TAPT unites with a Yeager-type configuration and then obtains protons and electrons for H₂O₂ production (Supplementary Fig. 32).

Discussion

In summary, we present a facile triple synergy for boosting H₂O₂ photosynthesis by an elaborately designed zwitterionic STT COF. Systematic investigations demonstrate that STT COF not only features a well-designed D-A configuration capable of improving the separation of photogenerated e[−]-h⁺ pairs, but also undergoes spontaneous hydrogenation to facilitate proton utilization and O₂ adsorption in Yeager-type configuration. As a result, a high H₂O₂ yield (14,356.5 μmol g^{−1} h^{−1}) with an AQY of 40.0% (at 420 nm) has been achieved over STT COF in pure water, outperforming its charge-neutral counterpart and other documented systems. A sunlight-driven continuous flow membrane reactor integrated with STT COF and gas diffusion layers achieves scalable production of 5 L of H₂O₂ (400 μM) within 7 h, demonstrating strong practical applicability. These findings underscore the significance of triple synergistic optimization of each successive reaction step of ORR, paving the avenue for efficient H₂O₂ photosynthesis.

Methods

Materials

4,4',4''-(1,3,5-Triazine-2,4,6-triyl)trianiline (TAPT, 98%), squaric acid (SQ, 98%) were obtained from Jilin Chinese Academy of Sciences-Yanshen Technology Co., Ltd. Terephthalaldehyde (PDA, 98%), N, N-

diethyl-1,4-phenylene-diamine sulfate (DPD, 96%), peroxidase (POD, horseradish, 99%), *p*-benzoquinone (*p*-BQ, 99%), potassium bromate (98%), isopropyl alcohol (IPA, AR), *n*-butyl alcohol (spectral pure), methylbenzene (AR), 1,2-dichlorobenzene (spectral pure), mesitylene (AR), sodium dihydrogen phosphate anhydrous (99%), potassium phosphate dibasic (99%), ferrous sulfate heptahydrate (99%), methyl blue (95%), bisphenol A (BPA, 99%), tetrahydrofuran (AR), *N*, *N*-dimethylformamide (DMF, AR), *n*-hexane (AR), methanol (MeOH, AR), acetic acid (AR), HCl (99%) and NaOH (98%) were purchased from Aladdin Co., Ltd., Shanghai, China. All chemicals were used without further purification. The carbon cloth (WIS1011) used for the continuous-flow membrane reactor was purchased from CeTech. The Ultrapure water (UP) with the resistivity of 18.3 MΩ cm^{−1} was used in this work.

Synthesis of COFs

The synthesis of STT COF. Squaric acid (25.1 mg, 0.22 mmol) and 4,4',4''-(1,3,5-triazine-2,4,6-triyl) trianiline (39.7 mg, 0.112 mmol) were mixed in a 10 mL pressure tube, then *n*-butyl alcohol (1.5 mL), methylbenzene (0.75 mL), and a suitable-sized magnetic stir bar were added. After 15 min of sonication, the mixture was degassed through three freeze-pump-thaw cycles and sealed under vacuum, then heated at 120 °C for 72 h with a rotation speed of 200 rpm. The obtained orange-colored sample was washed with DMF, tetrahydrofuran, water, and methyl alcohol. Finally, the products were evacuated at 60 °C under vacuum. The yield of STT COF is calculated to be ca. 89%.

The fabrication of PTT COF. PTT COF was synthesized according to a reported procedure with minor modifications⁵⁵. Typically, 4,4',4''-(1,3,5-triazine-2,4,6-triyl) trianiline (21.6 mg, 0.063 mmol), terephthalaldehyde (12.7 mg, 0.095 mmol), 1,2-dichlorobenzene (0.5 mL), *n*-butyl alcohol (0.5 mL), and acetic acid (0.1 mL, 6 M) were added to a 10 mL pressure tube. The mixture was sonicated for 15 min, followed by degassing through three freeze-pump-thaw cycles, vacuum sealing, and heating at 120 °C for 72 h. The obtained yellow sample was washed with tetrahydrofuran, DMF, and *n*-hexane. Finally, the products were evacuated at 60 °C in a vacuum drying oven overnight. The yield of PTT COF is ca. 92%.

Photocatalytic H₂O₂ production and other reactions

Photocatalytic H₂O₂ production. A flask was charged with the photocatalyst 5 mg, 20 mL of H₂O, and sealed with a septum. After thorough ultrasonication, the obtained suspension was degassed by O₂ bubbling for 20 min. Then the acquired solution was stirred in the dark for 30 min to establish equilibrium between absorption and desorption. A 300 W Xe lamp (PLSSXE300D/300DUV, Beijing Perfectlight, China) was used for the photocatalytic reaction. The entire reaction system was maintained at 25 °C using a cooling water system. At each sampling time, a syringe sampler was used to collect samples from the suspension, which were then immediately filtered through a 0.22 μm needle filter to remove the catalyst, resulting in a hydrogen peroxide solution ready for measurement.

Photocatalytic H₂O₂ decomposition. The evaluation of photocatalytic consumption of H₂O₂ involved dispersing 5 mg of COF-based catalysts in a 20 mL aqueous solution with 0.2 mM H₂O₂ under N₂ conditions.

Cycling experiments. To assess the photocatalytic stability of the catalyst, several parallel tests were conducted under identical conditions. After each cycle, the catalysts were separated and washed multiple times with methanol and water. The samples were then dried and reused in subsequent activity tests. This process was repeated for multiple cycles to evaluate the catalyst's performance over time.

Continuous flow membrane experiment. Gas diffusion layers (GDL) composed of carbon black and polytetrafluoroethylene (PTFE) were coated on one side of carbon cloth, which provides a high surface area and porosity to ensure efficient oxygen permeability⁵⁶. Then, a certain number of STT COF is coated on the other side of the carbon cloth.

Lab-setup reactor was applied with 100 mg STT COF, which was thoroughly dispersed within ethyl alcohol after 15 min of ultrasonication. Then the mixture was evenly coated on the carbon cloth (a circular area with a diameter of 10 cm) and left to naturally air-dry; it was fixed in the reactor. The reactor was charged with 200 mL of deionized water at the beginning of the experiment. The concentration of the produced H₂O₂ solutions was tested at specific time intervals. This experiment was conducted under UV-vis light irradiation.

A continuous flow membrane experiment under natural sunlight was conducted based on the above procedure, while the total amount of STT COF used was 4g, and the size of the carbon cloth was 40 cm × 40 cm. The pre-charged volume of deionized water is 1.6 L.

pH variation experiments. A quartz reactor was used to add 50 mg of COF and 20 mL of deionized water. After ultrasonication, the mixture was placed in a dark condition for 4 h. The experiment under light irradiation was carried on based on the usual route of photocatalytic H₂O₂ production in the main text.

Isotopic labeling experiment. STT COF (30 mg) was suspended in H₂O (10 mL) in a 20 mL glass vial. The suspension was well-dispersed by sonication for 5 min, then bubbled with ¹⁸O₂ for 10 min before sealing the vial. The reaction was irradiated for 6 h using a 300 W Xe lamp (320 nm < λ < 780 nm). The post-reaction photocatalytic hydrogen peroxide solution was transferred to a new vial, which was pre-vacuumed and charged with MnO₂. After the thorough decomposition of hydrogen peroxide, the evolved oxygen gas was analyzed through GC-MS (Agilent 8860-5977B).

Photocatalytic O₂ evolution. 5 mg of catalyst was charged in 20 mL of 0.01 M KBrO₃ solution, then 20 mg of La₂O₃ was added to maintain the pH⁵⁷. The experiment was conducted in an N₂ atmosphere under UV-vis light irradiation.

Fenton degradation. First of all, 10 mg L⁻¹ methyl blue containing 0.01 M FeSO₄ with pH = 3 was prepared. The configured methyl blue solution and the produced H₂O₂ solution (photocatalytic conditions: 20 mg of STT COF was placed in 20 mL of deionized water, exposed to O₂ for 20 min, and then reacted under UV-vis light for 2 h) were added in equal proportions, and the color change of methyl blue was observed.

As for bisphenol A (BPA) degradation, the procedure is similar to the above, except that the concentration of BPA is 5 mg L⁻¹, and the concentration of the pollutant is tested under liquid chromatography at a specific period.

Detection of H₂O₂ concentration

DPD colorimetry was used to detect the concentration of H₂O₂. The sodium phosphate buffer was prepared by slowly adding a 0.5 M sodium dihydrogen phosphate solution to a 0.5 M monosodium phosphate solution, monitoring the mixture until the pH reached 6. Additionally, 0.1g of DPD was dissolved in 10 mL of 0.05 M H₂SO₄. The other solution was prepared by adding 5 mg of POD to 5 mL of deionized water⁵⁸. To determine the H₂O₂ concentration, first fill a 10 mL colorimetric tube with 3 mL of phosphate buffer. Next, add a specific quantity of sample so that the absorbance falls within the standard curve. Next, sequentially add 50 μL of DPD solution and 50 μL of POD solution. Finally, use deionized water to bring the total volume to 10 mL and mix thoroughly. After stirring for 50 s, the absorbance at 551 nm was measured using a UV-vis spectrophotometer from Agilent

Technologies. Dilute the 30% H₂O₂ stock solution to a concentration of 0–200 μM, and use the colorimetric method to obtain the corresponding H₂O₂ concentration-absorbance standard curve. The linear relationship between the obtained H₂O₂ concentration and absorbance is shown in the Supplementary Fig. 33.

Characterization methods

The X-ray diffraction (XRD) pattern of samples was recorded on a Rigaku Smart Lab diffractometer with Cu Kα radiation (λ = 1.5418 Å) at room temperature. X-ray photoelectron spectroscopy (XPS) experiments were carried out using Thermo Fisher's ESCALAB 250Xi. Fourier transform infrared spectroscopy (FTIR) spectra were collected on a Nicolet iN10 (Thermo Fisher). Solid-state NMR spectra were obtained at the Bruker Avance III 400 MHz. The morphology of the sample was characterized on a field emission scanning electron microscope (FESEM, Zeiss Sigma 300, Gemini) and a transmission electron microscope (TEM, Tecnai G2-20, USA). Thermogravimetric analysis (TGA) was carried out on NETZSCH STA 449C by heating samples from 70 to 700 °C in a dynamic nitrogen atmosphere with a heating rate of 10 °C min⁻¹. The oxygen temperature-programmed desorption (O₂-TPD) test for the catalyst was conducted on an AutoChem II 2920. The photoluminescence (PL) tests were recorded on a F-4600 FL spectrophotometer at emission scan mode. In-situ diffuse reflectance infrared Fourier transform spectroscopy (DRIFTS) was carried out in Thermo IS 50. Temperature-dependent PL spectra (TD-PL) were explored on the Shimadzu RF-6000 spectrometer. EPR spectra were recorded on a Bruker EMX spectrometer. The pore size, pore volume, and surface area of samples were obtained by the Brunauer–Emmett–Teller (BET) instrument (ASAP 2460, Micromeritics). The concentration of bisphenol A was tested by High-Performance Liquid Chromatography (HPLC, Waters, USA). Concentrations of dissolved O₂ during the O₂ evolution experiment were tested by a portable oxygen dissolving meter (HACH, HQ 30 d). The Kelvin probe force microscopy (KPFM) (SPM-9700, Shimadzu, Japan) was used to test the surface potential of the samples. Ultraviolet-visible spectroscopy (UV-Vis-DRS) was performed by PerkinElmer Lambda 950. Electrochemical measurements were carried out on a CHI760e (Chenhua, Shanghai) electrochemical workstation in a three-electrode cell system. TA spectroscopy was performed using a commercial TA spectrometer (Helios, Ultrafast System, USA), with excitation provided by a femtosecond-pulsed amplifier (Astrella, 80 fs, 1 kHz, Coherent) and frequency-doubled by a Coherent Libra regenerative amplifier (800 nm, 80 fs, 1 kHz). Isotopic labeling experiments were analyzed through GC-MS (Agilent 8860-5977B).

Photoelectrochemical measurements and calculations of AQY

Photoelectrochemical characterizations. 10 mg of photocatalyst was added to 1 mL of ethanol. After 1 h of sonication, 20 μL of the mixture was applied onto the FTO conductive glass and dried to create a functioning electrode. The Ag/AgCl electrode served as the reference electrode, while the Pt electrode acted as the counter electrode. A 0.1 M Na₂SO₄ solution, freshly prepared before each experiment, was used as the electrolyte and analyzed using the electrochemical workstation (CHI760e, Shanghai Chenhua Instrument Co., Ltd.). A 300 W Xe lamp (420 nm < λ < 780 nm, PLSSXE300D/300DUV, Beijing Perfectlight, China) was used as the light source, and the transient photocurrent was measured over time during the on/off light cycle. The electrochemical impedance spectrum was evaluated across a frequency range from 1000 kHz to 0.01 Hz.

RRDE measurement. The RRDE experiments were carried out using a CHI760e electrochemical workstation in a standard three-electrode configuration. A RRDE electrode (glassy carbon disk with a platinum ring, disk area = 0.2475 cm²) was employed as the working electrode, with an Ag/AgCl electrode as the reference electrode and a graphite

rod as the counter electrode. The electrolyte was a 0.1M phosphate buffer solution (pH = 7), prepared fresh and used immediately for each experiment. The catalyst ink was prepared by dispersing 5 mg of the COF sample in 2 mL of isopropanol containing 50 μL of naphthol, followed by sonication for 30 min to obtain a homogeneous suspension. A fixed volume of the catalyst ink (10 μL) was drop-cast onto the surface of the RRDE and dried under ambient conditions. Before measurement, the electrolyte was saturated with O_2 by purging for at least 30 min. Linear sweep voltammetry (LSV) was employed to obtain the ORR polarization curves at a scan rate of $10 \text{ mV}\cdot\text{s}^{-1}$, with measurements taken at 1600 rpm. All measurements were conducted at room temperature. The number of transferred electrons (n) was calculated from the disk current (I_d) and ring current (I_r) using Eq. (1):

$$n = 4 \times \frac{I_d}{I_d + I_r/N} \quad (1)$$

where N is the Pt ring's collecting efficiency ($N = 0.37$), and I_d and I_r are the disk and ring currents (μA), respectively.

In-situ DRIFT measurements. For the tests in dark conditions, the samples were filled into an in-situ IR cell, and H_2O vapor was introduced into the cell. Before the measurement, the samples were degassed at 393 K for 6-h and then and then purged with Ar for 1 h at 353 K. The baseline was obtained after the samples had cooled down. The tests under photocatalytic conditions were started with Ar purging for 1 h at room temperature to remove the impurities. Next, moist oxygen (a mixture of oxygen and water vapor) was introduced in the dark, and the container was sealed to stop ventilation. The adsorption process lasted for 60 min, during which data were recorded at 30 min and 60 min until oxygen adsorption equilibrium was achieved. The reaction was then initiated by turning on the 300 W Xe lamp, and data were recorded at regular intervals.

Exciton dissociation energy calculation. Steady-state photoluminescence fluorescence (PL) spectra were recorded at different temperatures, and the E_b of the sample was calculated using the Arrhenius equation⁵⁹:

$$I(T) = \frac{I_0}{1 + A \exp\left(\frac{-E_b}{k_b T}\right)} \quad (2)$$

where I_0 represents the PL intensity at 0 K; T stands for temperature; k_b refers to Boltzmann's constant.

AQY measurement. The AQY of STT COF was tested in pure deionized water (30 mL) with a photocatalyst (20 mg) in a baker. Then, irradiated under Xe lamp (PLSSXE300D/300DUV, Beijing Perfectlight, China) at the wavelength of 420 nm for 30 min with magnetic stirring and continuous O_2 aeration. The active area of the reactor was approximately 7 cm^2 , and the light intensity was controlled to be 5 W m^{-2} . The AQY was calculated as follows:

$$\text{AQY} = \frac{(\text{number of } \text{H}_2\text{O}_2 \text{ production}) \times 2}{\text{number of incident photons}} \times 100\% \quad (3)$$

The number of incident photons is:

$$N_{\text{incident}} = \frac{Pt}{h\nu} = \frac{Pt\lambda}{hc} = \frac{ISt\lambda}{hc} \quad (4)$$

where I is the light power intensity (W m^{-2}), S is the irradiation area (m^2), t is the reaction time (s), λ is the wavelength length (m) of the monochromatic light, h is Planck's constant ($6.63 \times 10^{-34} \text{ m}^2 \text{ kg s}^{-1}$), and c is the speed of light in free space ($3.0 \times 10^8 \text{ m s}^{-1}$).

DFT calculations. Spin-polarized DFT calculations were performed utilizing the VASP 5.4.4⁶⁰, employing the projector-augmented wave (PAW)⁶¹ methodology. The Perdew–Burke–Ernzerhof (PBE) exchange–correlation functional⁶², within the generalized gradient approximation (GGA) framework, was adopted. A plane-wave kinetic energy cutoff of 450 eV and a Gaussian smearing width of 0.1 eV were implemented throughout the calculations. All atomic geometries and lattice vectors were optimized via the conjugate-gradient algorithm, with stringent convergence criteria set at 10^{-5} eV for total energy and $0.02 \text{ eV}/\text{\AA}$ for interatomic forces. The Brillouin zone was accomplished using a Γ -centered Monkhorst–Pack grid of $2 \times 2 \times 1$ grid for structural relaxation and a denser $4 \times 4 \times 1$ grid for self-consistent field (SCF) calculations. To avoid periodic artifacts, a 15 \AA vacuum layer was introduced. Dispersion corrections were accounted for via the DFT–D3 methodology to accurately describe van der Waals interactions⁶³. Charge redistribution was analyzed using:

$$\Delta\rho = \rho_{\text{tot}} - (\rho_{\text{part1}} + \rho_{\text{part2}}) \quad (5)$$

where ρ_{tot} is the total charge density, while ρ_{part1} and ρ_{part2} represent the charge densities of the correspond to isolated components. Visualization was performed with VESTA⁶⁴, and vibrational frequencies were obtained using VASPKIT⁶⁵.

The Gibbs free energy (ΔG) was evaluated as:

$$\Delta G = \Delta E + \Delta E_{\text{ZPE}} - T\Delta S \quad (6)$$

with ΔE from DFT, ΔE_{ZPE} from zero-point energy, and ΔS from vibrational analysis at 298.15 K (T). Entropies of gaseous H_2 and H_2O_2 were taken from the NIST database with standard conditions.

Optical excitations were studied using time-dependent DFT (TD-DFT) in Gaussian. Ground states were optimized at the B3LYP/6-311G(d) level, confirmed by frequency analysis. Excited states were calculated at CAM-B3LYP/6-311G(d) based on optimized geometries. Excited-state electron distributions were analyzed with Multiwfn (<http://sobereva.com/multiwfn>) and visualized in VESTA^{66,67}. Solvent effects were included via the conductor-like polarizable continuum model (C-PCM)⁶⁸, and Grimme's D3 correction was applied for dispersion⁶³.

Data availability

All the data supporting the findings of this study are available within the paper and its supplementary information files. Atomic coordinates of the optimized computational models of COFs are available in the Supplementary Data 1. Source data are provided with this paper.

References

- Zhao, Y. et al. Janus electrocatalytic flow-through membrane enables highly selective singlet oxygen production. *Nat. Commun.* **11**, 6228 (2020).
- Jiang, Y. et al. In situ turning defects of exfoliated Ti_3C_2 mxene into Fenton-like catalytic active sites. *Proc. Natl. Acad. Sci. USA* **120**, e2210211120 (2023).
- Richards, T. et al. A residue-free approach to water disinfection using catalytic in situ generation of reactive oxygen species. *Nat. Catal.* **4**, 575–585 (2021).
- Freese, T., Meijer, J. T., Feringa, B. L. & Beil, S. B. An organic perspective on photocatalytic production of hydrogen peroxide. *Nat. Catal.* **6**, 553–558 (2023).
- Liang, S. et al. Sustainable H_2O_2 production via solution plasma catalysis. *Proc. Natl. Acad. Sci. USA* **121**, e2410504121 (2024).
- García-Serna, J. et al. Engineering in direct synthesis of hydrogen peroxide: targets, reactors and guidelines for operational conditions. *Green Chem* **16**, 2320–2343 (2014).

7. Chen, L. et al. Acetylene and diacetylene functionalized covalent triazine frameworks as metal-free photocatalysts for hydrogen peroxide production: a new two-electron water oxidation pathway. *Adv. Mater.* **32**, 1904433 (2020).
8. Lin, Y.-J. et al. Thermocatalytic hydrogen peroxide generation and environmental disinfection by Bi₂Te₃ nanoplates. *Nat. Commun.* **12**, 180 (2021).
9. Yan, H. et al. Spontaneous exciton dissociation in organic photocatalyst under ambient conditions for highly efficient synthesis of hydrogen peroxide. *Proc. Natl. Acad. Sci. USA* **119**, e2202913119 (2022).
10. Shao, C. et al. Perfluoroalkyl-modified covalent organic frameworks for continuous photocatalytic hydrogen peroxide synthesis and extraction in a biphasic fluid system. *Nat. Commun.* **15**, 8023 (2024).
11. Liu, Y. et al. Enhanced hydrogen peroxide photosynthesis in covalent organic frameworks through induced asymmetric electron distribution. *Nat. Synth.* **4**, 134–141 (2024).
12. Tan, H. et al. Al-N₃ bridge site enabling interlayer charge transfer boosts the direct photosynthesis of hydrogen peroxide from water and air. *J. Am. Chem. Soc.* **146**, 31950–31960 (2024).
13. Chakraborty, A. et al. Enhancing photocatalytic hydrogen peroxide generation by tuning hydrazine linkage density in covalent organic frameworks. *Nat. Commun.* **16**, 503 (2025).
14. Peng, H. et al. Defective ZnIn₂S₄ nanosheets for visible-light and sacrificial-agent-free H₂O₂ photosynthesis via O₂/H₂O redox. *J. Am. Chem. Soc.* **145**, 27757–27766 (2023).
15. Ye, Y.-X. et al. Highly efficient photosynthesis of hydrogen peroxide in ambient conditions. *Proc. Natl. Acad. Sci. USA* **118**, e2103964118 (2021).
16. Teng, Z. et al. Atomically dispersed antimony on carbon nitride for the artificial photosynthesis of hydrogen peroxide. *Nat. Catal.* **4**, 374–384 (2021).
17. Luo, Y. et al. Sulfone-modified covalent organic frameworks enabling efficient photocatalytic hydrogen peroxide generation via one-step two-electron O₂ reduction. *Angew. Chem. Int. Ed.* **62**, e202305355 (2023).
18. Chi, W. et al. A photocatalytic redox cycle over a polyimide catalyst drives efficient solar-to-H₂O₂ conversion. *Nat. Commun.* **15**, 5316 (2024).
19. Li, L. et al. Custom-design of strong electron/proton extractor on COFs for efficient photocatalytic H₂O₂ production. *Angew. Chem. Int. Ed.* **63**, e202320218 (2024).
20. Zhao, W. et al. Accelerated synthesis and discovery of covalent organic framework photocatalysts for hydrogen peroxide production. *J. Am. Chem. Soc.* **144**, 9902–9909 (2022).
21. Li, Z. et al. Covalent organic frameworks for boosting H₂O₂ photosynthesis via the synergy of multiple charge transfer channels and polarized field. *Angew. Chem. Int. Ed.* **64**, e202420218 (2024).
22. Zhang, L., Wang, C., Jiang, Q., Lyu, P. & Xu, Y. Structurally locked high-crystalline covalent triazine frameworks enable remarkable overall photosynthesis of hydrogen peroxide. *J. Am. Chem. Soc.* **146**, 29943–29954 (2024).
23. Nath, I. et al. Mesoporous acridinium-based covalent organic framework for long-lived charge-separated exciton mediated photocatalytic [4+2] annulation. *Adv. Mater.* **37**, 2413060 (2025).
24. Krishnaraj, C. et al. Strongly reducing (diaryl-amino)benzene-based covalent organic framework for metal-free visible light photocatalytic H₂O₂ generation. *J. Am. Chem. Soc.* **142**, 20107–20116 (2020).
25. Tan, D. et al. Covalent organic frameworks enable sustainable solar to hydrogen peroxide. *Adv. Funct. Mater.* **34**, 2311655 (2024).
26. Yong, Z. & Ma, T. Solar-to-H₂O₂ catalyzed by covalent organic frameworks. *Angew. Chem. Int. Ed.* **62**, e202308980 (2023).
27. Liu, M., Xu, Q. & Zeng, G. Ionic covalent organic frameworks in adsorption and catalysis. *Angew. Chem. Int. Ed.* **63**, e202404886 (2024).
28. Kang, T. W. et al. An ion-channel-restructured zwitterionic covalent organic framework solid electrolyte for all-solid-state lithium-metal batteries. *Adv. Mater.* **35**, 2301308 (2023).
29. Jiang, G. et al. Lithium-ion accelerated regulators by locally-zwitterionic covalent organic framework nanosheets. *Adv. Energy Mater.* **14**, 2303672 (2024).
30. Fu, Y. et al. Zwitterionic covalent organic frameworks: attractive porous host for gas separation and anhydrous proton conduction. *ACS Nano* **15**, 19743–19755 (2021).
31. Zhai, L. et al. Constructing synergistic triazine and acetylene cores in fully conjugated covalent organic frameworks for cascade photocatalytic H₂O₂ production. *Chem. Mater.* **34**, 5232–5240 (2022).
32. Ben, H. et al. Local spatial polarization induced efficient charge separation of squaraine-linked COF for enhanced photocatalytic performance. *Adv. Funct. Mater.* **32**, 2104519 (2022).
33. Tao, Y. et al. Interlayer synergistic reaction of radical precursors for ultraefficient ¹O₂ generation via quinone-based covalent organic framework. *Proc. Natl. Acad. Sci. USA* **121**, e2401175121 (2024).
34. Yang, Y., Niu, H., Xu, L., Zhang, H. & Cai, Y. Triazine functionalized fully conjugated covalent organic framework for efficient photocatalysis. *Appl. Catal., B* **269**, 118799 (2020).
35. Qin, C. et al. Dual donor-acceptor covalent organic frameworks for hydrogen peroxide photosynthesis. *Nat. Commun.* **14**, 5238 (2023).
36. Wang, L. et al. A ZnO-based catalytic system for the synthesis of hydrogen peroxide from air. *Angew. Chem. Int. Ed.* **64**, e202424984 (2025).
37. Zhang, X. et al. Keto-anthraquinone covalent organic framework for H₂O₂ photosynthesis with oxygen and alkaline water. *Nat. Commun.* **15**, 2649 (2024).
38. Heppe, B. J., Dzombic, N., Keil, J. M., Sun, X.-L. & Ao, G. Solvent isotope effects on the creation of fluorescent quantum defects in carbon nanotubes by aryl diazonium chemistry. *J. Am. Chem. Soc.* **145**, 25621–25631 (2023).
39. Huang, Y. et al. Achieving a solar-to-chemical efficiency of 3.6% in ambient conditions by inhibiting interlayer charges transport. *Nat. Commun.* **15**, 5406 (2024).
40. Cheng, H. et al. Rational design of covalent heptazine frameworks with spatially separated redox centers for high-efficiency photocatalytic hydrogen peroxide production. *Adv. Mater.* **34**, 2107480 (2022).
41. Cheng, J. et al. Molecularly tunable heterostructured co-polymers containing electron-deficient and -rich moieties for visible-light and sacrificial-agent-free H₂O₂ photosynthesis. *Angew. Chem. Int. Ed.* **63**, e202406310 (2024).
42. Gao, T. et al. Electron-donating five-membered heterocyclic modulated electronic states boosting visible-light-driven H₂O₂ production. *Appl. Catal. B-Environ. Energy* **346**, 123761 (2024).
43. Liu, F. et al. Covalent organic frameworks for direct photosynthesis of hydrogen peroxide from water, air and sunlight. *Nat. Commun.* **14**, 4344 (2023).
44. Feng, S. et al. Rational design of covalent organic frameworks with redox-active catechol moieties for high-performance overall photosynthesis of hydrogen peroxide. *ACS Catal.* **14**, 7736–7745 (2024).
45. Guo, S. et al. Fully conjugated sp² carbon-linked covalent organic frameworks enables accelerated exciton process for superior singlet oxygen photosynthesis for water remediation. *Angew. Chem. Int. Ed.* **64**, e202509141 (2025).
46. Wang, S. et al. Efficient photocatalytic production of hydrogen peroxide using dispersible and photoactive porous polymers. *Nat. Commun.* **14**, 6891 (2023).

47. Lin, Z. et al. Diacetylene-bridged covalent organic framework as crystalline graphdiyne analogue for photocatalytic hydrogen evolution. *Chem. Sci.* **16**, 1948–1956 (2025).
48. Wang, A. et al. Enhanced and synergistic catalytic activation by photoexcitation driven S-scheme heterojunction hydrogel interface electric field. *Nat. Commun.* **14**, 6733 (2023).
49. Zhu, C. et al. Black hole quenchers for SERRS imaging of CXCR4 expression at single-cell level during treatment. *Adv. Funct. Mater.* **35**, 2417341 (2024).
50. Liu, R. et al. Linkage-engineered donor–acceptor covalent organic frameworks for optimal photosynthesis of hydrogen peroxide from water and air. *Nat. Catal.* **7**, 195–206 (2024).
51. Zhu, C. et al. Unveiling the dynamic evolution of single-atom Co sites in covalent triazine frameworks for enhanced H₂O₂ photosynthesis. *ACS Catal.* **14**, 2847–2858 (2024).
52. Chen, Y. et al. Hierarchical assembly of donor–acceptor covalent organic frameworks for photosynthesis of hydrogen peroxide from water and air. *Nat. Synth.* **3**, 998–1010 (2024).
53. Xue, F., Zhang, J. & Wang, Z. Precise modulation of conjugative structure and porosity in covalent organic frameworks for transition metal free visible-light catalysis of trifluoromethylation. *ACS Catal.* **14**, 5377–5388 (2024).
54. Qian, Y. et al. Computation-based regulation of excitonic effects in donor–acceptor covalent organic frameworks for enhanced photocatalysis. *Nat. Commun.* **14**, 3083 (2023).
55. Wang, H., Yang, C., Chen, F., Zheng, G. & Han, Q. A crystalline partially fluorinated triazine covalent organic framework for efficient photosynthesis of hydrogen peroxide. *Angew. Chem. Int. Ed.* **61**, e202202328 (2022).
56. Wang, W., Lu, Y., Luo, H., Liu, G. & Zhang, R. Effect of an improved gas diffusion cathode on carbamazepine removal using the electro-Fenton process. *RSC Adv.* **7**, 25627–25633 (2017).
57. Li, G. et al. Boosting exciton dissociation by regulating dielectric constant in covalent organic framework for photocatalysis. *Chem Catal.* **2**, 1734–1747 (2022).
58. Kou, M. et al. Molecularly engineered covalent organic frameworks for hydrogen peroxide photosynthesis. *Angew. Chem. Int. Ed.* **61**, e202200413 (2022).
59. Guan, X., Qian, Y., Zhang, X. & Jiang, H.-L. Enaminone-linked covalent organic frameworks for boosting photocatalytic hydrogen production. *Angew. Chem. Int. Ed.* **62**, e202306135 (2023).
60. Kresse, G. & Furthmüller, J. Efficient iterative schemes for AB initio total-energy calculations using a plane-wave basis set. *Phys. Rev. B* **54**, 11169–11186 (1996).
61. Blöchl, P. E. Projector augmented-wave method. *Phys. Rev. B* **50**, 17953–17979 (1994).
62. Perdew, J. P., Burke, K. & Ernzerhof, M. Generalized gradient approximation made simple. *Phys. Rev. Lett.* **77**, 3865–3868 (1996).
63. Grimme, S., Antony, J., Ehrlich, S. & Krieg, H. A consistent and accurate ab initio parametrization of density functional dispersion correction (DFT-D) for the 94 elements H–Pu. *J. Chem. Phys.* **132**, 154104 (2010).
64. Momma, K. & Izumi, F. Vesta 3 for three-dimensional visualization of crystal, volumetric and morphology data. *J. Appl. Cryst.* **44**, 1272–1276 (2011).
65. Wang, V., Xu, N., Liu, J.-C., Tang, G. & Geng, W.-T. Vaspkit: a user-friendly interface facilitating high-throughput computing and analysis using VASP code. *Comput. Phys. Commun.* **267**, 108033 (2021).
66. Lu, T. & Chen, F. Multiwfn: a multifunctional wavefunction analyzer. *J. Comput. Chem.* **33**, 580–592 (2012).
67. Liu, Z., Lu, T. & Chen, Q. An sp-hybridized all-carboatomic ring, cyclo[18]carbon: electronic structure, electronic spectrum, and optical nonlinearity. *Carbon* **165**, 461–467 (2020).
68. Barone, V. & Cossi, M. Quantum calculation of molecular energies and energy gradients in solution by a conductor solvent model. *J. Phys. Chem. A* **102**, 1995–2001 (1998).

Acknowledgements

This research is supported by the Basic Science Center Project of the National Natural Science Foundation of China (No. 52388101 to Z.F.Y.), the Program for Guangdong Introducing Innovative and Entrepreneurial Teams (No. 2019ZT08L213 to Z.F.Y.), and the National Natural Science Foundation of China (No. 22476028 to B.H.).

Author contributions

C.-C.L. and X.-M.L. completed most of the experiments and wrote the paper. B.C., Z.-F.L., Y.-H.L. (Yuhao Liu), C.-B.W., and S.Y. synthesized the catalyst and completed characterization. X.-W.Ou. carried out theoretical calculations and analysis. Y.-B.L., Y.-H.L. (Yunhai Liu), and L.-Q.Y. helped with the data interpretations. B.H. and Z.-F.Y. designed the experiments and supervised the project. All the authors discussed the results and commented on the manuscript.

Competing interests

The authors declare no competing interests.

Additional information

Supplementary information The online version contains supplementary material available at <https://doi.org/10.1038/s41467-025-63997-9>.

Correspondence and requests for materials should be addressed to Bin Han.

Peer review information *Nature Communications* thanks Jong-Pil Jeon, Beatriz Mourino, Pascal Van Der Voort and the other anonymous reviewer(s) for their contribution to the peer review of this work. A peer review file is available.

Reprints and permissions information is available at <http://www.nature.com/reprints>

Publisher's note Springer Nature remains neutral with regard to jurisdictional claims in published maps and institutional affiliations.

Open Access This article is licensed under a Creative Commons Attribution-NonCommercial-NoDerivatives 4.0 International License, which permits any non-commercial use, sharing, distribution and reproduction in any medium or format, as long as you give appropriate credit to the original author(s) and the source, provide a link to the Creative Commons licence, and indicate if you modified the licensed material. You do not have permission under this licence to share adapted material derived from this article or parts of it. The images or other third party material in this article are included in the article's Creative Commons licence, unless indicated otherwise in a credit line to the material. If material is not included in the article's Creative Commons licence and your intended use is not permitted by statutory regulation or exceeds the permitted use, you will need to obtain permission directly from the copyright holder. To view a copy of this licence, visit <http://creativecommons.org/licenses/by-nc-nd/4.0/>.

© The Author(s) 2025